RSC Advances

ROYAL SOCIETY OF CHEMISTRY

PAPER

View Article Online
View Journal | View Issue

Cite this: *RSC Adv.*, 2026, **16**, 1820

Fabrication of recycled dry cell electrode–derived graphene oxide/TiO_2/polyaniline composites and assessment of their photocatalytic and electrochemical performance

Md. Byzed Hasan, *[a] Sharmin Akter,[a] Abrar Yasir Abir,[a] Shamima Yesmin,[a] Shahidul Islam [b] and Md. Masud Parvez *[c]

The widespread use of synthetic dyes in textiles, paper, paints, and plastics causes severe water pollution by blocking sunlight, reducing photosynthesis, and harming ecosystems and human health. To mitigate this, graphene oxide (GO) was synthesized from waste dry cell electrodes, followed by the preparation of GO-incorporated titanium dioxide/polyaniline (GO/TiO_2/PANI) composites. The composites were then characterized for their structural and elemental properties using SEM, EDX, XRD and FTIR. The photocatalytic degradation of congo red dye was systematically examined under varying dye concentrations, pH levels, contact times, and catalyst dosages. At an initial concentration of 8 ppm, 92.7% degradation was achieved within 300 minutes under visible light irradiation at neutral pH. Catalyst dosage significantly influenced performance, with concentrations of 3, 5, 7, and 10 mg per 100 mL of an 8 ppm dye solution yielding degradation efficiencies of 80–85%, 92–95%, 96–98%, and 97–99%, respectively. Furthermore, electrochemical analysis demonstrated markedly enhanced performance, with the ternary composites exhibiting a specific capacitance of 17.50–43.87 F g^{-1}—substantially higher than that of individual GO, PANI, and PANI/TiO_2 systems. These findings demonstrate that the synthesized composite possesses enhanced photocatalytic activity, achieving efficient degradation of congo red dye under sunlight at neutral pH. The improved electrochemical performance obtained through GO incorporation further underscores the potential of recycled GO in developing electrode materials for supercapacitor applications. Moreover, the recycling of waste graphite into functional GO-based materials underscores the dual benefit of effective waste reduction and value-added material regeneration, paving the way for future research in environmental remediation and energy storage.

Received 5th October 2025
Accepted 19th December 2025

DOI: 10.1039/d5ra07587d

rsc.li/rsc-advances

1 Introduction

Water is a vital resource crucial for the survival of all living organisms and the sustenance of life on earth. However, rapid industrialization has resulted in the release of large amounts of organic and inorganic pollutants, heavy metals, dyes, pharmaceutical residues, and oil spills, leading to severe water contamination and increasing clean water scarcity.[1] In recent decades, semiconductor-based photocatalysis, an advanced oxidation process (AOP), has become a highly efficient, promising, and environmentally friendly method for the non-selective degradation of organic pollutants. Upon photo irradiation, the photocatalyst generates electron–hole pairs. These photoexcited electrons and holes react with oxygen (O_2), water (H_2O), and surface hydroxyl groups to produce reactive oxygen species (ROS) such as hydroxyl radicals ($^{\bullet}OH$) and superoxide anions ($O_2^{\bullet-}$) with strong oxidative power, which then attack and degrade organic pollutant molecules. Through photocatalytic oxidation, contaminants can be completely mineralized into harmless end products such as H_2O and CO_2, without producing secondary pollution. Its low energy demand and minimal maintenance requirements further enhance its appeal as a promising wastewater treatment strategy.[2–5] Common semiconductor-based metal oxide photocatalysts include TiO_2, ZnO, Fe_2O_3, SnO_2, WO_3, and CdS. Among these, TiO_2 is the most widely studied due to its suitable bandgap, simple synthesis process, low cost, strong photoactivity, excellent resistance to photocorrosion, high oxidizing power, and superior thermal stability.[6,7] However, metal oxide-based semiconductor photocatalysts face several challenges, such as narrow solar spectrum absorption, wide band gaps, and fast

---

[a] Department of Chemistry, Pabna University of Science and Technology, Pabna-6600, Pabna, Bangladesh. E-mail: byzed.che040@gmail.com; sharminakter19737@gmail.com; abirabraryasir@gmail.com; shamimayesmin857@gmail.com

[b] Department of Textile Engineering, BGMEA University of Fashion & Technology, Dhaka-1230, Bangladesh. E-mail: sulislam201@gmail.com

[c] Department of Chemistry, University of Barishal, Barishal-8254, Bangladesh. E-mail: masud.chdu@gmail.com

recombination of photogenerated electrons and holes, which limit their photocatalytic performance.[8] Recently, conducting organic polymers such as polyaniline (PANI), polypyrrole (PPy), and polythiophene (PTh) have also been reported to exhibit photocatalytic activity. However, pristine conducting polymers face challenges due to the high rate of electron–hole pair recombination, which limits their efficiency. In such cases, the photocatalytic efficiency can be greatly enhanced by creating composites of conducting organic polymers with metal oxides. Owing to their extended π-conjugated electron systems and narrower bandgaps compared to metal oxides, these polymers are capable of absorbing a broader spectrum of visible light. Photons with energy equal to or exceeding the HOMO–LUMO gap of the conducting polymer promote electrons (e^-) from the HOMO to the LUMO, leaving corresponding holes (h^+) in the HOMO. The excited electrons in the LUMO are transferred to the conduction band of the metal oxide, effectively separating the photogenerated charge carriers and delaying electron–hole recombination. The transferred electrons react with adsorbed water to form $O_2^{\bullet-}$ radicals, while the holes oxidize water to generate $^{\bullet}OH$ radicals.[9,10]

Polyaniline (PANI) is unique among conducting polymers due to its reversible electrical properties, changeable doping/dedoping behavior, simplicity of manufacturing, and environmental resilience.[11] PANI is commonly incorporated into composites with inorganic or organic semiconductors to extend visible-light absorption and facilitate photogenerated electron–hole separation, thereby enhancing photocatalytic performance,[12] and has been employed as a UV- or visible-light-driven photocatalyst for degrading cationic dyes such as rhodamine B,[13] malachite green,[14] and methylene blue,[14,15] as well as anionic dyes like congo red[16] and methyl orange.[17] Numerous studies have explored TiO_2 and conducting polymer nanocomposites, yet challenges with electron–hole recombination persist despite notable advancements. Adding graphene oxide (GO) to TiO_2-PANI composites decreases recombination by absorbing electrons from the TiO_2 surface. This electron absorption suppresses electron–hole recombination and enhances charge transfer and transport. Thereby, TiO_2/PANI/GO composites are expected to outperform pure TiO_2 and TiO_2/PANI composites in terms of photocatalysis. Kumar *et al.* prepared TiO_2/PANI/GO composites and observed significantly improved visible-light-driven degradation of the anionic dyes Rose Bengal and Thymol Blue, demonstrating that the incorporation of PANI and GO effectively enhanced TiO_2's photocatalytic efficiency.[11] Husain *et al.* synthesized *in situ* assembled GO/TiO_2/PANI nanocomposites for the photocatalytic degradation of benzene and toluene. The GO/TiO_2/PANI composite showed exceptional photocatalytic performance, removing 99.81% of benzene and 99.16% of toluene under optimized conditions (pH 9, 90 min, 60 ppm, 0.2 g adsorbent) upon UV-Vis irradiation.[18]

Furthermore, to address growing energy demands, supercapacitors have gained significant attention as electrochemical energy storage devices due to their high-power density, fast charge–discharge capabilities, and outstanding cycle life stability.[19] PANI-based transition metal oxide composites, incorporating high-surface-area carbonaceous materials such as graphene oxide, are attracting significant interest as supercapacitor electrode material.

In this study, TiO_2/PANI and TiO_2/PANI/GO composites were synthesized *via in situ* oxidative polymerization using a reduced amount of $FeCl_3$ as the oxidant. The graphene oxide (GO) utilized in this work was derived from graphite recovered from used dry cells, supporting a circular-economy-based material sourcing approach. To the best of our knowledge, this is the first comprehensive investigation to utilize spent dry-cell-derived GO for the fabrication of TiO_2-PANI-GO composites and to explore their photocatalytic and electrochemical properties. The synthesized materials were characterized using FTIR, UV-Vis spectroscopy, XRD, EDX, and SEM techniques. In addition, their thermal stability and decomposition behavior were assessed through thermogravimetric analysis (TGA). Photocatalytic performance was evaluated through the degradation of the azo dye Congo Red (CR) under sunlight irradiation. The influence of key operational parameters—including solution pH, dye concentration, and catalyst dosage—was systematically examined to determine their effects on degradation efficiency. Additionally, the its electrochemical performance of the synthesized composites was evaluated using cyclic voltammetry (CV), galvanostatic charge–discharge (GCD), and electrochemical impedance spectroscopy (EIS).

2 Materials and methods

2.1 Chemicals and reagents

The required chemical reagents included concentrated sulfuric acid (H_2SO_4, 98%), *ortho*-phosphoric acid (H_3PO_4, 85%), hydrogen peroxide (H_2O_2, 30%), hydrochloric acid (HCl, 37%), concentrated nitric acid (HNO_3), potassium permanganate ($KMnO_4$), titanium dioxide (TiO_2), ferric chloride ($FeCl_3$), aniline ($C_6H_5NH_2$), ethanol, and Congo red. All chemicals were of analytical grade and used as received, without further purification.

2.2 Preparation of graphite powder from discarded battery electrodes

Graphite electrodes were separated from spent batteries and thoroughly washed with distilled water. To remove surface contaminants such as MnO_2, residual metals, and oily deposits, the electrodes were gently polished with sandpaper and repeatedly rinsed with distilled water. The cleaned electrodes were then crushed and ground into a fine graphite powder. The resulting powder was treated with a 3 : 1 mixture of hydrochloric acid (HCl) and nitric acid (HNO_3) to eliminate residual impurities. The suspension was magnetically stirred at 40 °C for approximately 2 hours to ensure effective dissolution of contaminants. After cooling, the mixture was centrifuged, and the recovered graphite powder was washed several times with distilled water until a neutral pH was obtained. The collected graphite powder was dried at 50 °C for 24 hours and subsequently in a vacuum oven for complete moisture removal.

2.3 Synthesis of GO from recovered graphite powder

Graphene oxide (GO) was synthesized from graphite powder using an Improved Hummers Method. A mixture of concentrated sulfuric acid (H_2SO_4) and *ortho*-phosphoric acid (H_3PO_4) in a 9 : 1 ratio (97.5 mL H_2SO_4 and 32.5 mL H_3PO_4) was prepared and cooled in an ice bath with continuous stirring for 15 minutes. Then, 1 g of graphite powder was added, and the mixture was sonicated for 40 minutes. The solution was then returned to the ice bath after sonication, and 3 g of potassium permanganate ($KMnO_4$) was gradually added while maintaining the temperature below 5 °C. The mixture was then stirred at 50 °C for 5 hours.

The reaction mixture was allowed to cool to room temperature and was left to stand overnight. The oxidation was then quenched by adding 200 mL of cold deionized water, followed by 0.9 mL of 30% hydrogen peroxide (H_2O_2) to remove any residual $KMnO_4$. The product was washed repeatedly with 20% hydrochloric acid (HCl), deionized water, and ethanol *via* centrifugation until a neutral pH was achieved. The purified GO powder was finally obtained following drying at 50 °C.

2.4 Synthesis of GO-TiO_2-PANI composites

Waste-battery-derived graphene oxide (GO) incorporated TiO_2-PANI composites were synthesized *via* an *in situ* one-pot method. The composites were prepared with a fixed 150 mg of TiO_2, while the GO content was varied from 3 to 9 wt% (relative to TiO_2) and the aniline amount was maintained at ten times the combined weight of TiO_2 and GO. For GO/TiO_2/PANI-1, GO/TiO_2/PANI-2, GO/TiO_2/PANI-3, and GO/TiO_2/PANI-4, the corresponding GO/aniline quantities were 13.5 mg/1.635 g, 10.5 mg/1.605 g, 7.5 mg/1.575 g, and 4.5 mg/1.545 g, respectively. A TiO_2/PANI composite (without GO) was also synthesized using 1.5 g of aniline. Composite synthesis was carried out by first mixing required amount of aniline with 15 mL of 1 N HCl in a beaker and stirring magnetically for 1 hour to obtain a homogeneous solution. The required amounts of GO and TiO_2 were subsequently incorporated into the mixture and sonicated to ensure uniform dispersion. In a separate beaker, $FeCl_3$ (equal to half the weight of aniline) was dissolved in 10 mL of HCl, and the solution was then gradually introduced into the main reaction mixture to initiate polymerization (Scheme 1).

The reaction mixtures were continuously stirred with a magnetic stirrer for 24 hours to complete the polymerization. Afterward, the reaction was stopped, and the resulting solution was repeatedly centrifuged with deionized water and ethanol until the acid and low-molecular-weight oligomers were completely removed. The composites were then dried using a vacuum evaporator, followed by oven drying at 50 °C.

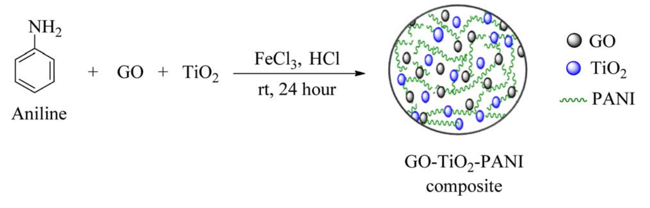

Scheme 1 Reaction scheme for the preparation of GO/TiO_2/PANI composites.

2.5 Material characterization

FTIR spectra were recorded using a Bruker Alpha II FTIR spectrophotometer (Bruker Optik GmbH & Co., Germany) in attenuated total reflection mode (ATR-FTIR). The spectra were collected in the mid-IR region (600–4000 cm^{-1}) with a resolution of 2 cm^{-1} in transmittance mode. UV-Vis spectra were acquired using a Shimadzu UV-1800 spectrophotometer across the 200–800 nm range. Thermal stability was evaluated using a thermogravimetric analyzer (TGA; Seiko Instruments Inc., Japan, model EXSTAR-6000) by monitoring weight loss from room temperature to 800 °C at a heating rate of 20 °C min^{-1} under a nitrogen atmosphere. Morphological and elemental analyses were carried out using a ZEISS Sigma 300 FESEM coupled with a Bruker XFlash 630M energy-dispersive X-ray (EDX) detector (Germany). X-ray diffraction (XRD) patterns were obtained using a Panalytical X'Pert Pro diffractometer (Model PW3040/60, The Netherlands) with Cu Kα radiation (λ = 1.5406 Å), operated at 40 kV and 30 mA. Diffraction data were recorded over a 2θ range of 5°–80° at a scanning rate of 2.4° 2θ/min, and the resulting diffractograms were used to determine the crystalline properties of the samples.

2.6 Photocatalytic experiments

For the degradation studies, 100 mL of Congo red solution (8 ppm) was placed in conical flasks, each containing 5 mg of the respective catalyst. Before sunlight exposure, the mixtures were magnetically stirred in the dark for 30 minutes to achieve adsorption–desorption equilibrium between the dye molecules and the photocatalyst. During irradiation, the suspensions were continuously stirred to keep the catalyst particles well dispersed. At regular time intervals, aliquots of the reaction mixture were withdrawn and centrifuged at 1500 rpm for 5 minutes to separate the catalyst. The resulting supernatant was analyzed at $\lambda_{\max} = 497$ nm using a Shimadzu UV-1800 spectrophotometer to monitor the degradation of Congo red.

The amount of Congo red removed has been calculated by the following equation:

$$\%\text{ of removal} = \left[\frac{C_i - C_f}{C_i}\right] \times 100\%$$

where C_i represents the initial absorbance of Congo red, and C_f denotes the absorbance at a given time interval during the photocatalytic degradation process.

2.7 Electrode preparation

A three-electrode electrochemical setup was used, comprising a graphite rod as the working electrode, Ag/AgCl as the reference electrode, and a platinum wire as the counter electrode. The catalyst was deposited onto the graphite rod surface *via* a drop-casting technique. For slurry preparation, 10 mg of the synthesized material was mixed with 100 µL of *N*-methyl-2-pyrrolidone (NMP) and 5% polyvinylidene fluoride (PVDF) solution, followed by sonication to ensure uniform dispersion. A 10 μL aliquot of the slurry was then applied onto the glassy carbon rods using a micropipette, and the modified electrodes were dried at 80 °C for 60 minutes. The calculated active masses (excluding PVDF) were 1.6 mg for PANI, 1.4 mg for PANI-TiO_2, 1.6 mg for GO, and 1.2, 1.2, 1.3, and 1.4 mg for the 3%, 5%, 7%, and 9% composites, respectively.

2.8 Electrochemical analysis

The fabricated composites were evaluated for their supercapacitor performance. Galvanostatic charge–discharge (GCD) tests were conducted within the potential window of −0.3 to +0.5 V at a fixed current density of 1.0 A g^{-1}, using the same electrode after cyclic voltammetry (CV) measurements. All electrochemical measurements were carried out in a 1.0 M KOH electrolyte solution at 25 °C. To investigate the effect of current density, GCD curves were also recorded in the range of 1.0–5.0 A g^{-1} for GO, PANI, PANI/TiO_2, and GO/TiO_2/PANI composite-coated graphite electrodes. Electrochemical impedance spectroscopy (EIS) was carried out for all three fabricated electrodes in the frequency range of 5×10^{-2} to 5×10^{5} Hz, with a scan rate of 50 mV s^{-1}. The EIS data were analyzed using CS Studio software. The specific capacitance (C_s) of each electroactive sample was measured from the GCD curves using the following equation:

$$C_{\mathrm{s}} = \frac{I \times \Delta t}{m \times \Delta v}$$

where ΔV represents the discharge potential excluding the IR drop, m is the mass (g) of the active material coated on the electrode, I is the applied discharge current (A), and Δt is the corresponding discharge time (s).

3 Results and discussion

3.1 Structural characterization

3.1.1 Spectral analysis. Fig. 1a shows the FT-IR spectra of recovered graphite from dry cell electrodes and the graphene oxide (GO) synthesized from this recovered graphite. The nearly flat transmittance curve of graphite indicates the absence of significant surface functional groups. In comparison, the FT-IR spectrum of GO exhibits a broad absorption band at 3356 cm^{-1}, which is associated with O–H stretching vibrations, along with a peak at 1388 cm^{-1} that corresponds to the bending vibrations of hydroxyl (–OH) groups.[20] A prominent spectral feature at 1718 cm^{-1} corresponds to the carbonyl stretch C═O of carboxylic acid functionalities present in the material.[21] Another prominent peak at 1595 cm^{-1} was observed, corresponding to the C═C stretching vibration of sp^2-hybridized carbon in aromatic or conjugated structures within unoxidized graphitic domains.[22,23] The absorption bands at 1202 cm^{-1} and 1057 cm^{-1} are linked to C–O stretching vibrations associated with the C–OH group and the C–O–C moiety in epoxy rings, respectively, whereas the band at 957 cm^{-1} is indicative of the presence of epoxy or peroxide groups.[24,25] These spectral characteristics confirm that the recovered graphite was successfully oxidized to graphene oxide.

FTIR spectra of pure PANI (Fig. 1b) shows a noticeable absorption peak at 3440 cm^{-1}. This peak corresponds to the N–H bond's stretching vibration, which is characteristic of the amino groups present in the PANI structure. The C═C and C═N stretching modes for the benzenoid and quinoid rings are shown by the peaks at 1480 and 1540 cm^{-1}, respectively. The aromatic ring's out-of-plane C–H bending is attributed to the band at 800 cm^{-1}.[26] Aromatic C–N stretching produces the peak at 1230 cm^{-1}. Protonation of PANI causes peaks at 1120 cm^{-1}, which are characteristic bands.[27] The C═N stretching band in the TiO_2/PANI composite appears at a slightly higher wavenumber (around 1568 cm^{-1}) compared to that of pure PANI, which suggests possible interactions between TiO_2 and the nitrogen atoms of polyaniline. As a transition metal oxide, TiO_2 can coordinate with nitrogen atoms (forming Ti–N interactions), which may weaken the native C═N and C═C bonds in PANI, leading to the observed shifts in the corresponding FTIR peak positions.[28] The FT-IR spectra of the GO/TiO_2/PANI composite show similarities to those of both GO and TiO_2/PANI, suggesting that graphene oxide was successfully added to the composites. In contrast to pure GO, the bands at 1670 cm^{-1}

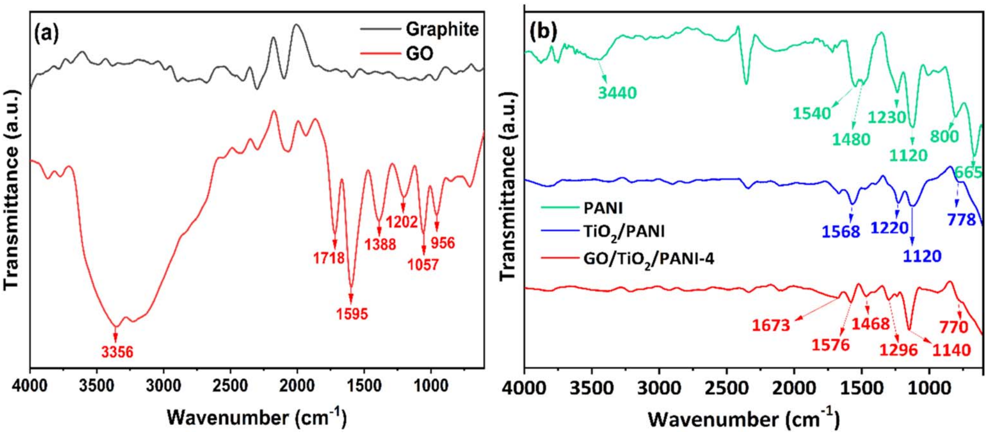

Fig. 1 FT-IR spectra of (a) Graphite and Graphene oxide (GO) and (b) polyaniline, TiO_2/PANI composites, and GO/TiO_2/PANI-4 composites.

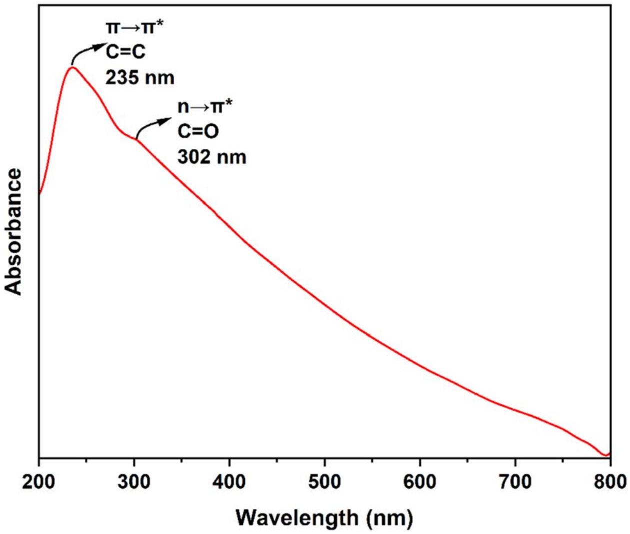

Fig. 2 UV-Vis absorption spectrum of graphene oxide (GO) in aqueous dispersion, highlighting characteristic π → π* and n → π* transitions.

indicates a change in the C═O stretching and interactions between GO and TiO_2. The C═N peak in the GO/TiO_2/PANI composites shifts to 1576 cm^{-1}. The peaks at 1576 cm^{-1} and 1468 cm^{-1} confirm that aromatic structure of PANI remains unchanged. This shift occurs due to the inclusion of TiO_2 into the PANI matrix.[29] Furthermore, bands at 1296 cm^{-1} (C–N stretching of the benzenoid ring) and the absorption signals at around 770 cm^{-1} are characteristic of the Ti–O–Ti lattice.[30]

The UV-visible spectrum of the aqueous dispersion of graphene oxide (GO), as shown in Fig. 2, displays two distinct absorption features: a prominent peak at 235 nm, arising from π → π* transitions of aromatic C═C bonds, and a shoulder at 302 nm, associated with to n → π* transitions of C═O functional groups.[20]

3.1.2 Energy Dispersive X-ray (EDX) analysis. The synthesis of GO was further confirmed by elemental analysis of graphite and graphene oxide (GO) using the Energy Dispersive X-ray (EDX) method. In graphite, the atomic fractions of C and O were 90.29% and 8.79%, respectively, while in GO, the values were 62.16% and 35.93%. The EDX study shows material changes from graphite to graphene oxide. Graphite contains little oxygen, but graphene oxide has substantial oxygen functionalization, which improves its dispersibility and reactivity. These percentages of C and O were calculated from the intensity of the characteristic lines and are summarized in Table 1.

Table 1 Elemental composition of Graphite and Graphene oxide (GO)

Graphite		Graphene oxide	
Element	Weight (%)	Element	Weight (%)
C	90.29	C	62.16
O	8.79	O	35.93
S	0.88	S	1.90
Mn	0.04	Mn	0.02

3.1.3 X-ray diffraction (XRD) analysis. XRD analysis (Cu-Kα radiation, 2θ range 0–80°) was carried out to investigate the structural characteristics. The diffraction patterns of GO, PANI, and TiO_2/PANI, and GO/TiO_2/PANI-4 composites are shown in Fig. 3.

Two minor diffraction peaks appear at $2\theta = 25.21°$ and 33.25°, and the absence of any sharp crystalline reflections indicates that the polymer matrix is predominantly amorphous in nature. The average particle size was determined using the Debye–Scherrer equation based on the full width at half maximum (FWHM) of the diffraction peaks, as shown in the following.[31]

$$D = \frac{k\lambda}{\beta \cos\theta}$$

Where, β is the full width at half maximum (FWHM), λ is the wavelength (nm) of the incident beam, θ is the Bragg angle, k is the Scherrer constant (0.9), and "D" is the crystallite size (nm). The average crystallite size of polyaniline calculated is 8.0 nm.

The XRD pattern of the synthesized graphene oxide (GO) exhibits a prominent diffraction peak at $2\theta = 10.57°$, which corresponds to the (001) plane of GO, indicating successful oxidation and exfoliation of graphite. During the synthesis of graphene oxide, residual domains of intact graphitic structure or partially oxidized graphite may persist, giving rise to a weak (002) diffraction peak near 26.79°, despite the majority of the material being oxidized. A lower intensity peak observed at $2\theta = 42.45°$ may correspond to turbostratic band of disordered carbon materials.[20,23,32] These features confirm the successful synthesis of GO from discarded battery graphite using a modified Hummers' method. The average crystallite size of Graphene oxide calculated is 8.3 nm. GO/TiO_2/PANI-4 exhibits XRD peaks at $2\theta = 27.65°$, 36.31°, 41.43°, 54.53°, 56.85°, 62.97°, 64.29°, and 69.23°, corresponding to the (110), (101), (111), (211), (220), (002), (310), and (301) crystal planes of rutile TiO_2. "In the GO/TiO_2/PANI composite, a slight decrease in peak intensity along with a small shift in the TiO_2 peaks is observed. These variations are likely due to the interactions among GO, TiO_2, and PANI chains, as well as the reduced volume fraction of TiO_2 in the composite compared to bulk TiO_2.[18,33] Due to the strong crystalline nature of TiO_2, the characteristic amorphous peaks of PANI and GO are not observed in the GO/TiO_2/PANI composites, as the intense TiO_2 diffraction peaks can mask the weaker signals associated with GO and PANI. The average crystallite size of GO/TiO_2/PANI-4 composite calculated is 16.9 nm.

3.1.4 Microscopic analysis. The morphologies of graphite, graphene oxide, TiO_2, PANI, and GO/TiO_2/PANI-4 composites are characterized by SEM analysis at higher magnifications (150.00 KX). Fig. 4a presents the SEM image of graphite, revealing large, dense, and smooth layered platelets with minimal exfoliation. The distinct stacked lamellar morphology is typical of bulk graphite and reflects the presence of tightly packed graphitic layers. GO, on the other hand, exhibits a highly wrinkled, crumpled, leaf-like sheet morphology with a porous structure [Fig. 4b], resulting from oxidation and exfoliation of graphite *via* the improved Hummer's method. This structure provides increased surface area and abundant active sites,

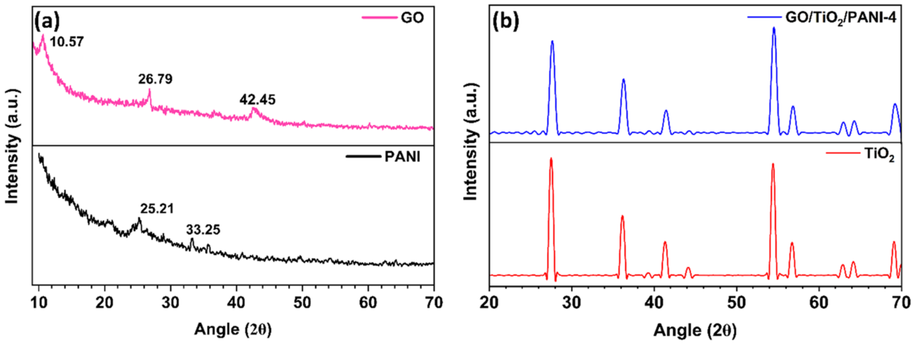

Fig. 3 XRD patterns depicting the crystalline features of (a) GO and PANI, and (b) TiO_2 and the GO/TiO_2/PANI-4 composite.

favorable for composite formation. PANI exhibits a porous, sponge-like network consisting of interconnected fibrous and globular structures, whereas the TiO_2 sample displays particles of nearly spherical shapes [Fig. 4c and d, respectively]. Fig. 4e illustrates that the GO/TiO_2/PANI composite possesses a cohesive, multi-phase architecture, with TiO_2 and PANI distributed on the GO sheets. The composite material features a porous morphology and enhanced surface roughness.

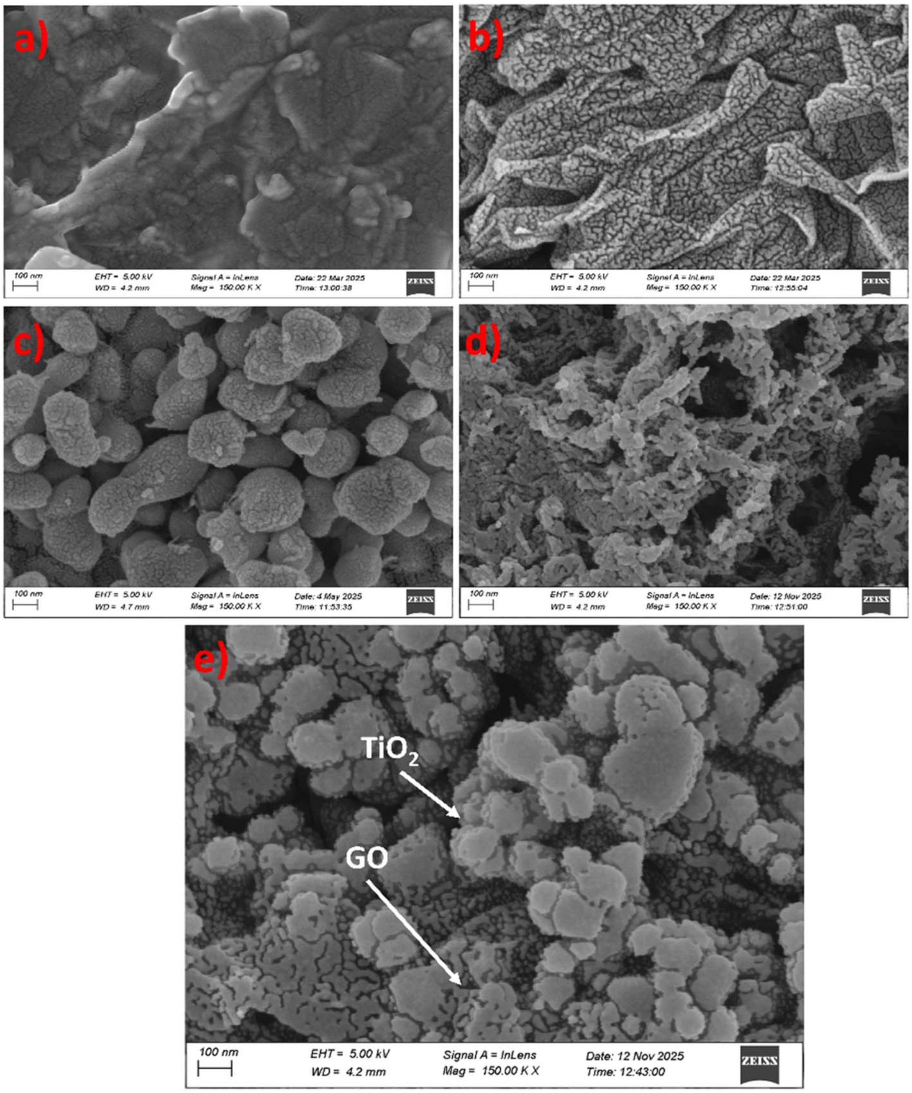

Fig. 4 SEM image of (a) Graphite, (b) GO, (c) TiO_2, (d) PANI, and (e) GO/TiO_2/PANI-4 composites.

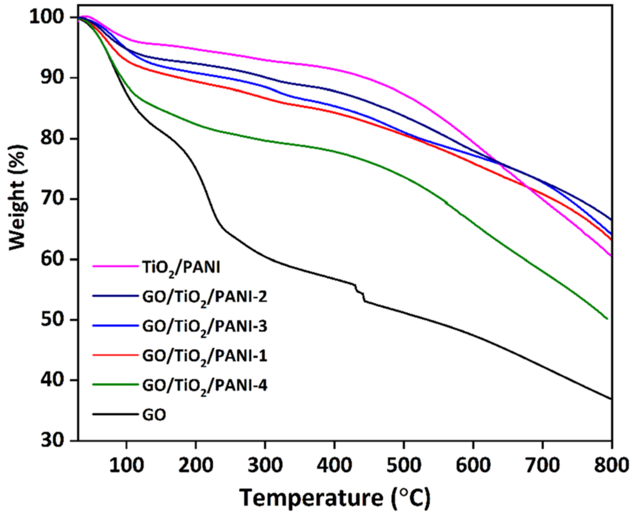

Fig. 5 Thermogravimetric analysis of GO, TiO_2/PANI, and the GO/TiO_2/PANI composites.

3.2 Thermogravimetric (TGA) analysis

Thermogravimetric analysis was conducted to assess the thermal stability of GO, TiO_2/PANI composites, and GO/TiO_2/PANI composites, as presented in Fig. 5. The TGA curve of GO exhibits three major weight loss stages. The initial weight loss observed below 150 °C corresponds to the desorption of physically adsorbed water on the material surface. A considerable weight loss occurs between 190 °C and 250 °C, corresponding to the decomposition of thermally unstable oxygen-containing functional groups such as hydroxyl, epoxy, and carboxyl groups. The gradual weight loss up to 800 °C is associated with the decomposition of more stable oxygenated functional groups, including carbonyl and ether groups, which were formed on the GO surface during the oxidation process.[34,35] TiO_2/PANI composites show a moderate weight reduction, with major degradation occurring between 300 °C and 600 °C, while the initial weight loss below 150 °C is due to the evaporation of moisture and residual solvent. In contrast, GO/TiO_2/PANI-1, GO/TiO_2/PANI-2, and GO/TiO_2/PANI-3 composites display minimal weight loss in the 200–600 °C range, indicating good thermal stability. However, GO/TiO_2/PANI-4 composite undergoes two distinct decomposition stages. The initial weight loss below 120 °C is attributed to the removal of water and ethanol molecules adsorbed on the polymer surface. The second stage, occurring below 500 °C, is mainly attributed to the decomposition of oxygen-containing functional groups (–COOH, –OH, *etc.*) in GO. Compared to TiO_2/PANI and the lower-GO composites (GO/TiO_2/PANI-1, GO/TiO_2/PANI-2, and GO/TiO_2/PANI-3), GO/TiO_2/PANI-4 exhibits reduced thermal stability, which can be ascribed to the higher content of thermally labile oxygenated groups introduced by GO. Therefore, it is evident that increasing the GO content leads to greater weight loss in PANI–GO–TiO_2 composites.

3.3 Band gap analysis

To estimate the optical band gap energy (Eg), the powdered samples were first dispersed in deionized water and sonicated to obtain a homogeneous solution. The UV-Vis spectra were recorded for the resulting dispersion. The optical band gaps of GO, PANI, TiO_2, TiO_2/PANI, and various GO/TiO_2/PANI composites were then determined using Tauc plots, where $(\alpha h\nu)^2$ is plotted against the photon energy ($h\nu$) for direct allowed transitions. The linear portion of each plot was extrapolated to intersect the energy axis, yielding the corresponding band gap values. In this context, α is the absorption coefficient, $h\nu$ is the photon energy, and Eg denotes the optical band gap. The results indicate that GO and PANI exhibit relatively wide band gaps of 3.58 eV and 3.36 eV, respectively, while TiO_2 shows a band gap of 3.11 eV. The incorporation of PANI

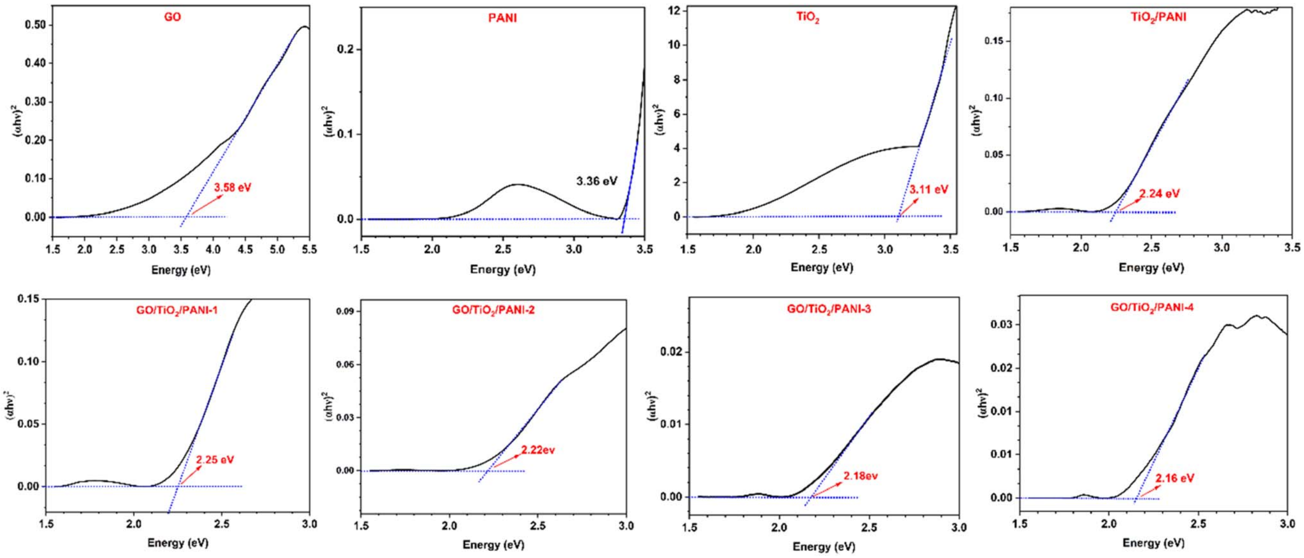

Fig. 6 Tauc plots for evaluating the direct allowed band gap (Eg) of GO, TiO_2, PANI, TiO_2/PANI, and GO/TiO_2/PANI composites.

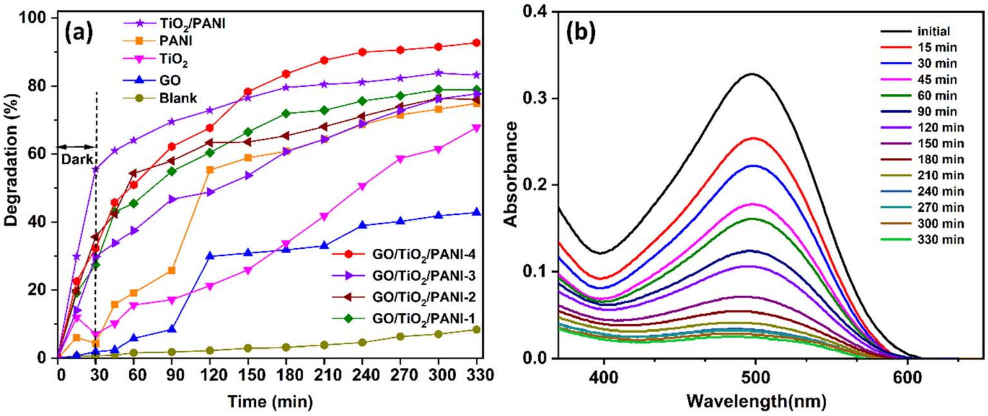

Fig. 7 (a) Time-dependent degradation efficiency of the synthesized composite materials compared with their individual (bare) components. (b) Absorption spectral changes of Congo Red solution during sunlight-driven photocatalysis using the GO/TiO_2/PANI-4 composite.

into TiO_2 reduces the band gap to 2.24 eV, and further inclusion of GO in ternary GO/TiO_2/PANI composites progressively narrows the band gaps from 2.25 eV to 2.16 eV with increasing GO content. These results suggest that the formation of ternary composites effectively narrows the optical band gap, potentially enhancing visible-light absorption and photocatalytic performance (Fig. 6).

3.4 Photocatalytic activity

3.4.1 Effect of contact time. The photocatalytic activity of the individual materials (GO, PANI, TiO_2) and the TiO_2/PANI and GO/TiO_2/PANI composites toward Congo Red degradation was assessed by monitoring UV-Visible absorption spectra under sunlight irradiation in the presence of the synthesized photocatalysts. Fig. 7a depicts the degradation of an 8 ppm Congo Red dye solution using 5 mg of each catalyst at neutral pH, showing a progressive decrease in dye concentration over time. The study of the GO/TiO_2/PANI ternary composites indicates that increasing the GO content enhances photocatalytic and oxidative dye degradation, with the GO/TiO_2/PANI-4 composite exhibiting the highest degradation efficiency. Among all samples, GO/TiO_2/PANI-4 reached a photodegradation efficiency of 92.7%, demonstrating the highest photocatalytic activity (Fig. 8). Therefore, this composite was selected for further experiments to investigate the effects of pH, dye concentration, and catalyst dosage.

3.4.2. Effect of pH. The degradation efficiency trend across pH values is probably impacted by the way the dye molecules engage with the composite (GO/TiO_2/PANI) under various acidic and alkaline circumstances. Fig. 9 presents the degradation of congo red dye after a 30-minute dark equilibration followed by 270 minutes of sunlight irradiation. The composite exhibited the highest degradation efficiency at neutral pH, suggesting that neutral conditions are optimal for its catalytic activity. Although pH 5 and 7 showed comparable efficiencies, higher pH values led to reduced performance. This may be attributed to the fact that at alkaline pH, the higher concentration of hydroxyl ions can impart additional negative charge to the catalyst surface. Since Congo Red is an anionic dye, this charge buildup induces repulsive interactions that hinder dye adsorption, thereby reducing the overall catalytic efficiency.

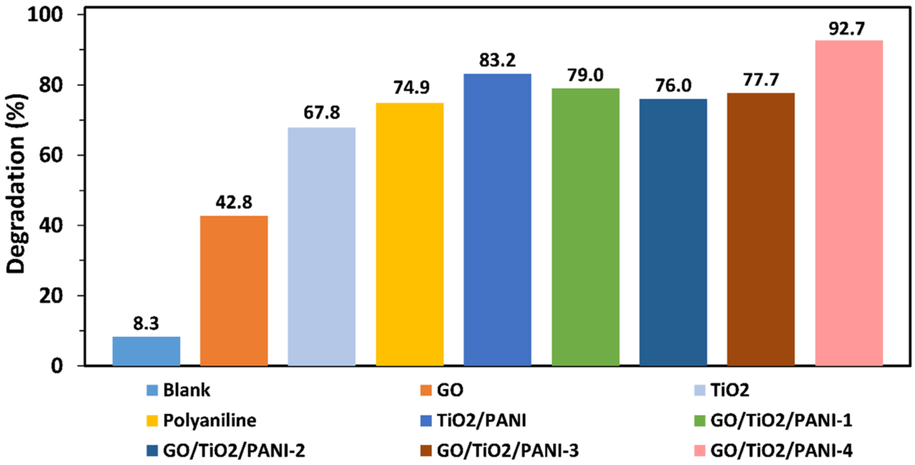

Fig. 8 Degradation efficiency of various catalysts—including individual components (GO, TiO_2, PANI), TiO_2/PANI, and GO/TiO_2/PANI composites—under sunlight after 300 minutes using 5 mg of catalyst with 8 ppm Congo Red solution.

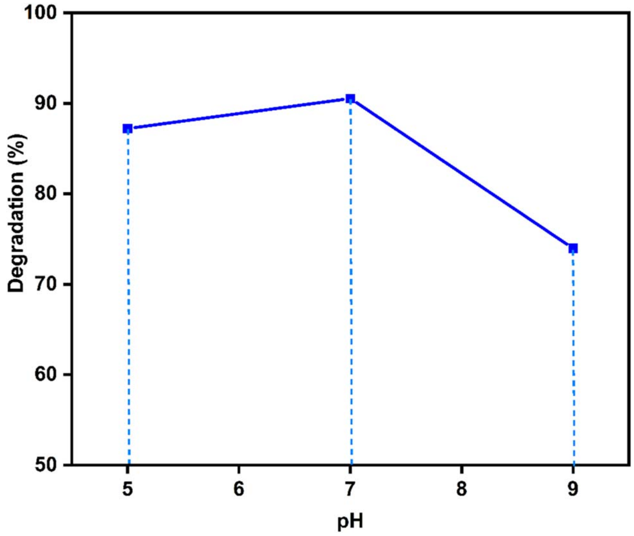

Fig. 9 Effect of solution pH on the photocatalytic degradation efficiency of congo red (CR) dye using the GO/TiO_2/PANI-4 composite.

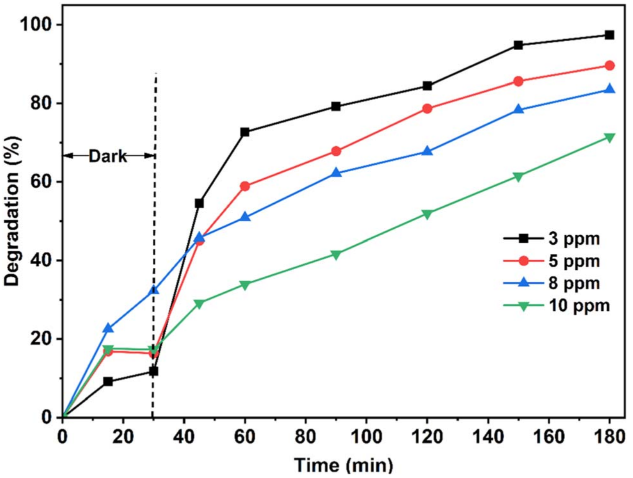

Fig. 11 Effect of initial dye concentration on the photocatalytic degradation efficiency of the dye using the GO/TiO_2/PANI-4 composite.

3.4.3. Effect of catalyst dosage. The photocatalytic performance of GO/TiO_2/PANI-4 was evaluated by varying the catalyst dosage (3, 5, 7, and 10 mg) in an 8 ppm congo red solution at pH 7. The degradation efficiency increased with catalyst dosage, as higher amounts provide more active sites on the photocatalyst surface, generating a greater number of reactive oxygen species.[36] Higher catalyst doses (7 mg and 10 mg) exhibited maximum photocatalytic activity, while lower doses (3 mg and 5 mg) showed moderate activity. Using 10 mg of catalyst, a degradation efficiency of 97.5% was achieved within 210 minutes (Fig. 10).

3.4.4. Effect of concentration. The effect of dye concentration on photocatalytic degradation was investigated under visible light using 5 mg of catalyst with congo red solutions of varying concentrations (3, 5, 8, and 10 ppm). At lower dye concentrations, the degradation rate increased proportionally with substrate concentration. However, at higher concentrations, the catalyst's efficiency declined due to factors such as increased dye adsorption on the catalyst surface, reduced light penetration from screening effects, limited generation of OH$^{\bullet}$ and O2$-^{\bullet}$ radicals for a given light intensity and catalyst amount, dye molecule aggregation, and reduced availability of active sites.[37] The GO/TiO_2/PANI-4 composite exhibited the highest degradation at a dye concentration of 3 ppm, achieving 97.4% within 180 minutes (Fig. 11).

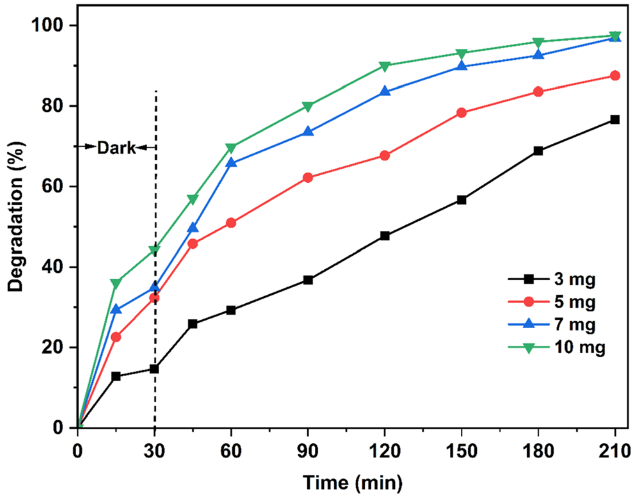

Fig. 10 Influence of catalyst dosage on the photocatalytic degradation of congo red dye.

3.4.5 Photodegradation mechanism of Congo red dye by GO/TiO_2/PANI composites. The GO/TiO_2/PANI combination effectively degrades Congo Red dye using light-induced catalytic reactions. When exposed to light, GO/TiO_2/PANI composite absorbs photons, forming electron–hole pairs. Photogenerated electrons are transferred to GO and PANI, while TiO_2 retains the photoinduced holes, thereby reducing electron–hole recombination. Consequently, graphene oxide (GO) and polyaniline (PANI) enhance charge separation and electron transport, effectively minimizing recombination losses.[18] The excited electrons combine with dissolved oxygen (O_2) to produce superoxide radicals ($O_2^{\bullet -}$), while the holes oxidize water and hydroxide ions to form hydroxyl radicals ($^{\bullet}OH$). These reactive oxygen species initiate the oxidative degradation of Congo Red. After oxidation, the dye molecules are mineralized into CO_2, H_2O, and other non-toxic byproducts such as N_2 and NH_3 (Fig. 12). This ensures effective color removal while supporting sustainable wastewater treatment. The corresponding photochemical reactions involved in this process are as follows:

$$\text{GO/TiO}_2\text{/PANI} + h\nu \rightarrow \text{GO/TiO}_2\text{/PANI}\ (e^- + h^+)$$

$$e^- + O_2 \rightarrow O_2^{\bullet -}$$

$$O_2^{\bullet -} + H^+ \rightarrow HOO^{\bullet}$$

$$h^+ + OH^- \rightarrow +\ OH^{\bullet}$$

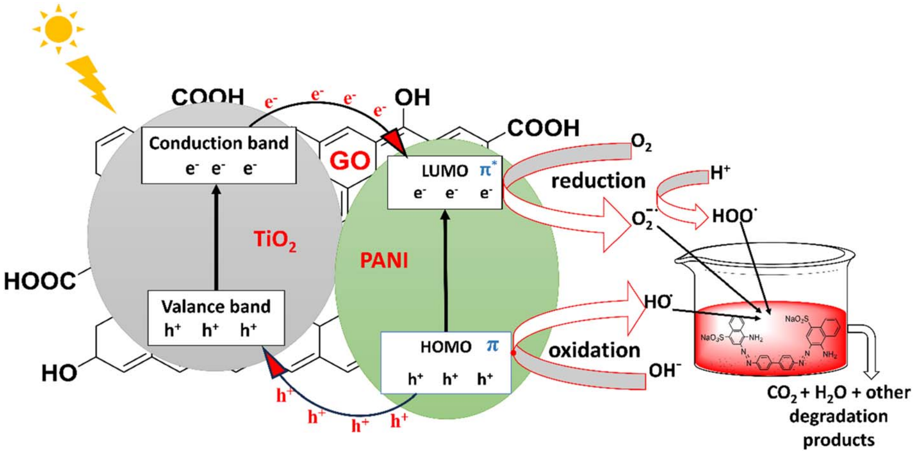

Fig. 12 Schematic illustration of the proposed photocatalytic degradation mechanism of Congo Red dye using the GO/TiO_2/PANI composite.

$$\mathrm{GO/TiO_2/PANI + CR \rightarrow CR_{adsorbed}}$$

$$\mathrm{CR_{adsorbed} + OH^{\bullet} + HOO^{\bullet} + O_2^{\bullet -} + \rightarrow CO_2 + H_2O + other\ degradation\ products}$$

3.5 Electrochemical properties

3.5.1 Electrochemical impedance spectroscopy (EIS) study. EIS was used to examine the modified electrode's capacity to transport electrons. Fig. 13 shows electrochemical impedance Nyquist plots of in 1 M KOH solution. The corresponding equivalent circuit is depicted in the inset, with Rs representing the coating layer resistance and Rct indicating the charge transfer resistance. The parallel combination of the constant phase element (CPE) and Rct corresponds to the charge-transfer-limiting process.

Table 2 presents the electrochemical impedance spectroscopy (EIS) parameters of PANI, GO, and their synthesized composites (GO/PANI/TiO_2) measured at a frequency range from 1×10^5 Hz to 1×10^{-2} in 1 M KOH solution. The parameters include solution resistance (R_s), charge transfer resistance (R_{ct}), and constant phase element (CPE). Solution resistance (R_s) values remain relatively close for all samples, ranging between 1.84–2.22 Ω, suggesting a negligible difference in electrolyte resistance.

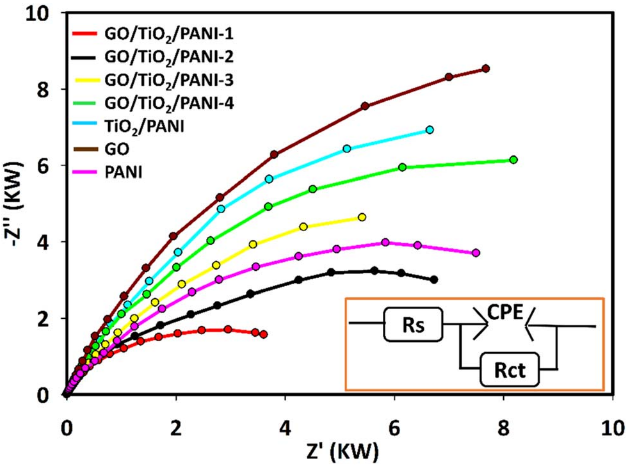

Fig. 13 The EIS Nyquist plots of PANI, GO and the synthesized composites recorded at a potential of 0.55 V in experimental conditions in 1 M KOH solution.

However, notable variations are observed in the charge transfer resistance (R_{ct}). PANI (34 430 Ω) and TiO_2/PANI (27 247 Ω) exhibit the highest R_{ct} values, indicating sluggish charge transfer kinetics. In contrast, the GO/PANI/TiO_2 composites show a remarkable reduction in Rct, with GO/PANI/TiO_2-1 presenting the lowest value (4023 Ω), suggesting enhanced conductivity and faster interfacial charge transfer. This improvement is further supported by its smallest semicircle in the Nyquist plot (Fig. 13), confirming enhanced electrical conductivity of this electrode.

The CPE values vary from 4.58×10^{-4} to 7.77×10^{-4} F. Incorporation of GO and TiO_2 generally increases capacitance, with GO/PANI/TiO_2-4 exhibiting the highest value (7.77×10^{-4} F).

Overall, the results indicate that introducing GO and TiO_2 into PANI significantly improves electrochemical performance by lowering charge transfer resistance and increasing capacitance, which is beneficial for supercapacitor applications.

3.5.2 Cyclic voltammetry (CV) study. The charge storage performance of the synthesized composites was analyzed using cyclic voltammetry (CV) at a scan rate of 50 mV s^{-1}. Based on the

Table 2 EIS properties of PANI, GO and the synthesized composites recorded in 1 M KOH solution

Modified electrode	R_s (Ω)	R_{ct} (Ω)	CPE (F)
GO	1.91	34 430	6.17×10^{-4}
PANI	1.84	11 397	4.58×10^{-4}
TiO_2/PANI	1.98	27 247	5.29×10^{-4}
GO/TiO_2/PANI-1	2.17	4023	7.31×10^{-4}
GO/TiO_2/PANI-2	2.05	9152	6.83×10^{-4}
GO/TiO_2/PANI-3	1.93	14 774	4.79×10^{-4}
GO/TiO_2/PANI-4	2.22	20 050	7.77×10^{-4}

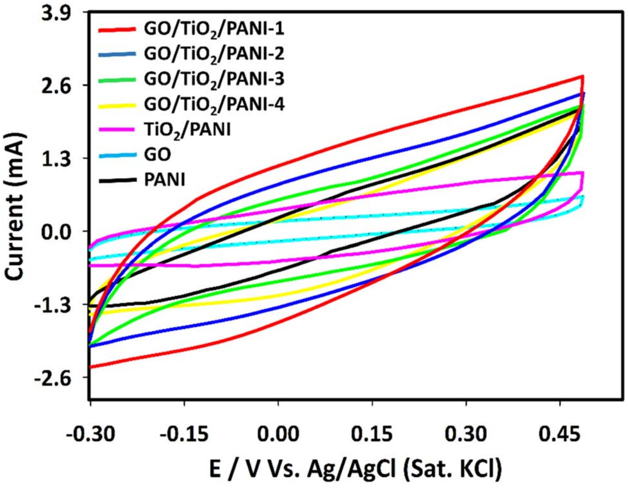

Fig. 14 Cyclic voltammograms curves of PANI, GO and the synthesized composites at 500 mVs^{-1} scan rate.

CV results presented in Fig. 14, the incorporation of GO into the composite significantly enhances the charge storage performance, as evidenced by the larger enclosed area and higher current response.

Among all the tested samples, GO/TiO_2/PANI-1 exhibits the highest current response, indicating enhanced charge storage capacity due to the strong synergistic effect between GO, PANI, and TiO_2. The other GO/TiO_2/PANI composites also show enhanced activity compared to pure GO, PANI and TiO_2/PANI, though their performance is slightly lower than GO/TiO_2/PANI1, highlighting the importance of an optimized composition. In contrast, PANI and TiO_2/PANI deliver moderate responses, while GO alone exhibits the lowest current response with nearly linear behavior, confirming its limited capacitive contribution. The integration of GO, PANI, and TiO_2 exhibits a strong synergistic effect, positioning GO/TiO_2/PANI-1 as the most effective electrode material for energy storage systems.

3.5.3 GCD study. The galvanostatic charge–discharge (GCD) curves (Fig. 15) obtained from the three-electrode cell, where the composite-modified graphite rods served as working electrodes, together with the electrochemical performance data (Table 3), reveal that the GO/TiO_2/PANI composites deliver improved energy storage performance compared to their individual constituents and binary systems. From the GCD profiles, GO/TiO_2/PANI-1 exhibits the longest discharge time, corresponding to the highest specific capacitance of 43.87 F g^{-1} and a discharge duration of 42.11 s. In contrast, pure GO and PANI, with capacitances of 6.63 F g^{-1} and 9.38 F g^{-1}, respectively, exhibit much shorter discharge times (8.49 s and 12 s), indicating limited charge storage and poor stability. The binary system TiO_2/PANI (10.38 F g^{-1}, 11.63 s) shows slight improvement over bare GO and PANI but still falls short compared to the ternary composites. Among the GO/TiO_2/PANI series, performance decreases with increasing GO content, as observed in GO/TiO_2/PANI-2 (34.48 F g^{-1}, 33.1 s), GO/TiO_2/PANI-3 (22.40 F g^{-1}, 23.3 s), and GO/TiO_2/PANI-4 (17.50 F g^{-1}, 18.2 s). This trend highlights the importance of optimizing the GO, PANI, and TiO_2 ratio to achieve balanced supercapacitor performance.

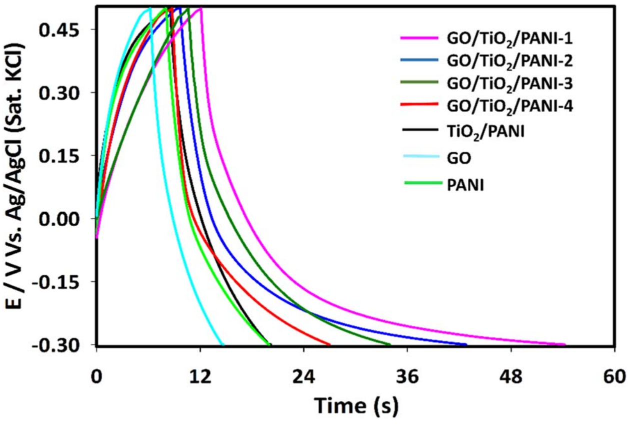

Fig. 15 Galvanostatic charge/discharge curves for electrodes modified with PANI, GO, TiO_2 and PANI/GO/TiO_2 composites.

Table 3 Specific capacitance, and discharging time value of PANI, GO, TiO_2 and GO/TiO_2/PANI composites

Modified electrode	Specific capacitance (Fg^{-1})	Discharging time (s)
GO	6.63	8.49
PANI	9.38	12
TiO_2/PANI	10.38	11.63
GO/TiO_2/PANI-1	43.87	42.11
GO/TiO_2/PANI-2	34.48	33.1
GO/TiO_2/PANI-3	22.40	23.3
GO/TiO_2/PANI-4	17.50	18.2

4 Conclusion

This study successfully demonstrates the synthesis and application of a graphene oxide-based composite (GO/TiO_2/PANI) derived from recycled dry cell electrodes for dual-functional use in photocatalysis and energy storage. The composite demonstrated remarkable photocatalytic activity for the degradation of Congo Red dye. Using 10 mg of catalyst, a degradation efficiency of 97.5% was achieved within 210 minutes under visible light at neutral pH, with the performance influenced by catalyst dosage, pH, and contact time. Structural and electrochemical analyses confirmed the material's improved performance, with high specific capacitance, outperforming individual components and binary composites. The integration of waste-derived graphene oxide not only enhances environmental sustainability through pollutant degradation but also adds value through its potential in supercapacitor applications. These findings highlight GO/TiO_2/PANI as a promising, eco-friendly material for wastewater treatment and energy storage, opening avenues for scalable and sustainable environmental technologies.

Author contributions

Md. Byzed Hasan: writing – original draft, conceptualization, methodology, investigation, data curation, supervision. Sharmin Akter: writing – original draft, methodology, investigation.

Abrar Yasir Abir: investigation, writing – review & editing. Shamima Yesmin: writing – original draft, investigation. Shahidul Islam: writing – review & editing, data curation. Md. Masud Parvez: writing – review & editing, data curation, supervision.

Conflicts of interest

The authors declare that they have no conflict of interest.

Data availability

All data generated or analyzed during this study are included in this published article.

Acknowledgements

The author(s) received no financial support for the research, authorship, and/or publication of this article.

References

1 S. Mishra and B. Sundaram, A review of the photocatalysis process used for wastewater treatment, *Mater. Today: Proc.*, 2024, **102**, 393–409, DOI: 10.1016/j.matpr.2023.07.147.

2 Y.-J. Lee, H. S. Lee, C.-G. Lee, S.-J. Park, J. Lee, S. Jung and G.-A. Shin, Application of PANI/TiO2 Composite for Photocatalytic Degradation of Contaminants from Aqueous Solution, *Appl. Sci.*, 2020, **10**, 6710, DOI: 10.3390/app10196710.

3 S. Mishra and B. Sundaram, A review of the photocatalysis process used for wastewater treatment, *Mater. Today: Proc.*, 2024, **102**, 393–409, DOI: 10.1016/j.matpr.2023.07.147.

4 F. Anjum, M. Shaban, M. Ismail, S. Gul, E. M. Bakhsh, M. A. Khan, U. Sharafat, S. B. Khan and M. I. Khan, Novel Synthesis of CuO/GO Nanocomposites and Their Photocatalytic Potential in the Degradation of Hazardous Industrial Effluents, *ACS Omega*, 2023, **8**, 17667–17681, DOI: 10.1021/acsomega.3c00129.

5 F. T. Geldasa, M. A. Kebede, M. W. Shura and F. G. Hone, Experimental and computational study of metal oxide nanoparticles for the photocatalytic degradation of organic pollutants: a review, *RSC Adv.*, 2023, **13**, 18404–18442, DOI: 10.1039/D3RA01505J.

6 Y. Yue, X. Yue, X. Tang, L. Han, J. Wang, S. Wang and C. Du, Synergistic adsorption and photocatalysis study of TiO2 and activated carbon composite, *Heliyon*, 2024, **10**, e30817, DOI: 10.1016/j.heliyon.2024.e30817.

7 G. A. Snook, P. Kao and A. S. Best, Conducting-polymer-based supercapacitor devices and electrodes, *J. Power Sources*, 2011, **196**, 1–12, DOI: 10.1016/j.jpowsour.2010.06.084.

8 F. T. Geldasa, M. A. Kebede, M. W. Shura and F. G. Hone, Experimental and computational study of metal oxide nanoparticles for the photocatalytic degradation of organic pollutants: a review, *RSC Adv.*, 2023, **13**, 18404–18442, DOI: 10.1039/D3RA01505J.

9 R. Kumar, J. Travas-Sejdic and L. P. Padhye, Conducting polymers-based photocatalysis for treatment of organic contaminants in water, *Chem. Eng. J. Adv.*, 2020, **4**, 100047, DOI: 10.1016/j.ceja.2020.100047.

10 G. Saianand, A.-I. Gopalan, L. Wang, K. Venkatramanan, V. A. L. Roy, P. Sonar, D.-E. Lee and R. Naidu, Conducting polymer based visible light photocatalytic composites for pollutant removal: Progress and prospects, *Environ. Technol. Innovation*, 2022, **28**, 102698, DOI: 10.1016/j.eti.2022.102698.

11 A. Kumar, C. J. Raorane, A. Syed, A. H. Bahkali, A. M. Elgorban, V. Raj and S. C. Kim, Synthesis of TiO2, TiO2/PAni, TiO2/PAni/GO nanocomposites and photodegradation of anionic dyes Rose Bengal and thymol blue in visible light, *Environ. Res.*, 2023, **216**, 114741, DOI: 10.1016/j.envres.2022.114741.

12 S. Rafiq, M. A. Lovely, S. R. Mim, M. S. Islam, M. Hasan and M. M. Billah, Structure controlled enhanced photocatalytic activity of polyaniline (PANI), *Heliyon*, 2025, **11**, e42888, DOI: 10.1016/j.heliyon.2025.e42888.

13 S. Majumdar and D. Mahanta, Deposition of an ultra-thin polyaniline coating on a TiO_2 surface by vapor phase polymerization for electrochemical glucose sensing and photocatalytic degradation, *RSC Adv.*, 2020, **10**, 17387–17395, DOI: 10.1039/D0RA01571G.

14 V. Eskizeybek, F. Sarı, H. Gülce, A. Gülce and A. Avcı, Preparation of the new polyaniline/ZnO nanocomposite and its photocatalytic activity for degradation of methylene blue and malachite green dyes under UV and natural sun lights irradiations, *Appl. Catal., B*, 2012, **119–120**, 197–206, DOI: 10.1016/j.apcatb.2012.02.034.

15 R. Thekkayil, P. Gopinath and H. John, Enhanced photocatalytic activity of polyaniline through noncovalent functionalization with graphite oxide, *Mater. Res. Express*, 2014, **1**, 045602, DOI: 10.1088/2053-1591/1/4/045602.

16 J. Miao, A. Xie, S. Li, F. Huang, J. Cao and Y. Shen, A novel reducing graphene/polyaniline/cuprous oxide composite hydrogel with unexpected photocatalytic activity for the degradation of Congo red, *Appl. Surf. Sci.*, 2016, **360**, 594–600, DOI: 10.1016/j.apsusc.2015.11.005.

17 Y. Cheng, L. An, Z. Zhao and G. Wang, Preparation of polyaniline/TiO2 composite nanotubes for photodegradation of AZO dyes, *J. Wuhan Univ. Technol., Mater. Sci. Ed.*, 2014, **29**, 468–472, DOI: 10.1007/s11595-014-0941-4.

18 S. Husain, S. A. Muhammad, K. A. Ali, M. Saquib Tanweer and N. Ahmad, In-situ assembled GO/TiO2 and GO/TiO2/PANI nanocomposites for the enhanced photocatalytic degradation of benzene and toluene, *Polym. Bull.*, 2025, **82**, 12707–12729, DOI: 10.1007/s00289-025-06027-4.

19 M. B. Poudel, C. Yu and H. J. Kim, Synthesis of Conducting Bifunctional Polyaniline@Mn-TiO2 Nanocomposites for Supercapacitor Electrode and Visible Light Driven Photocatalysis, *Catalysts*, 2020, **10**, 546, DOI: 10.3390/catal10050546.

20 I. Roy, G. Sarkar, S. Mondal, D. Rana, A. Bhattacharyya, N. R. Saha, A. Adhikari, D. Khastgir, S. Chattopadhyay and

D. Chattopadhyay, Synthesis and characterization of graphene from waste dry cell battery for electronic applications, *RSC Adv.*, 2016, **6**, 10557–10564, DOI: 10.1039/C5RA21112C.

21 T. F. Emiru and D. W. Ayele, Controlled synthesis, characterization and reduction of graphene oxide: A convenient method for large scale production, *Egypt. j. basic appl. sci.*, 2017, **4**, 74–79, DOI: 10.1016/j.ejbas.2016.11.002.

22 M. S. Akhtar, D. S. R. Jutt, S. Aslam, R. Nawaz, M. A. Irshad, M. Khan, M. Khairy, A. Irfan, S. A. Al-Hussain and M. E. A. Zaki, Green synthesis of graphene oxide and magnetite nanoparticles and their arsenic removal efficiency from arsenic contaminated soil, *Sci. Rep.*, 2024, **14**, 23094, DOI: 10.1038/s41598-024-73734-9.

23 P. B. Sreelekshmi, R. R. Pillai and A. P. Meera, Controlled Synthesis of Novel Graphene Oxide Nanoparticles for the Photodegradation of Organic Dyes, *Top. Catal.*, 2022, **65**, 1659–1668, DOI: 10.1007/s11244-022-01600-x.

24 D. He, Z. Peng, W. Gong, Y. Luo, P. Zhao and L. Kong, Mechanism of a green graphene oxide reduction with reusable potassium carbonate, *RSC Adv.*, 2015, **5**, 11966–11972, DOI: 10.1039/C4RA14511A.

25 K. Pan, T. Leng, J. Song, C. Ji, J. Zhang, J. Li, K. S. Novoselov and Z. Hu, Controlled reduction of graphene oxide laminate and its applications for ultra-wideband microwave absorption, *Carbon N Y*, 2020, **160**, 307–316, DOI: 10.1016/j.carbon.2019.12.062.

26 S. S. Umare, B. H. Shambharkar and R. S. Ningthoujam, Synthesis and characterization of polyaniline-Fe3O4 nanocomposite: Electrical conductivity, magnetic, electrochemical studies, *Synth. Met.*, 2010, **160**, 1815–1821, DOI: 10.1016/j.synthmet.2010.06.015.

27 U. M. Chougale, J. V. Thombare, V. J. Fulari and A. B. Kadam, Synthesis of polyaniline nanofibres by SILAR method for supercapacitor application, in: *2013 International Conference on Energy Efficient Technologies for Sustainability, ICEETS 2013*, 2013, pp. 1078–1083. doi: DOI: 10.1109/ICEETS.2013.6533537.

28 V. Gilja, K. Novaković, J. Travas-Sejdic, Z. Hrnjak-Murgić, M. K. Roković and M. Žic, Stability and synergistic effect of polyaniline/TiO2 photocatalysts in degradation of Azo dye in wastewater, *Nanomaterials*, 2017, **7**(12), 412, DOI: 10.3390/nano7120412.

29 S. Baruah, S. Kumar, B. Nayak and A. Puzari, Optoelectronically suitable graphene oxide-decorated titanium oxide/polyaniline hybrid nanocomposites and their enhanced photocatalytic activity with methylene blue and rhodamine B dye, *Polym. Bull.*, 2021, **78**, 1703–1720, DOI: 10.1007/s00289-020-03182-8.

30 J. Tian, G. Yang, D. Jiang, F. Su and Z. Zhang, A hybrid material consisting of bulk-reduced TiO2, graphene oxide and polyaniline for resistance based sensing of gaseous ammonia at room temperature, *Microchim. Acta*, 2016, **183**, 2871–2878, DOI: 10.1007/s00604-016-1912-6.

31 G. Vinodha, P. D. Shima and L. Cindrella, Mesoporous magnetite nanoparticle-decorated graphene oxide nanosheets for efficient electrochemical detection of hydrazine, *J. Mater. Sci.*, 2019, **54**, 4073–4088, DOI: 10.1007/s10853-018-3145-z.

32 F. Anjum, M. Shaban, M. Ismail, S. Gul, E. M. Bakhsh, M. A. Khan, U. Sharafat, S. B. Khan and M. I. Khan, Novel Synthesis of CuO/GO Nanocomposites and Their Photocatalytic Potential in the Degradation of Hazardous Industrial Effluents, *ACS Omega*, 2023, **8**, 17667–17681, DOI: 10.1021/acsomega.3c00129.

33 M. Sasikumar and N. P. Subiramaniyam, Microstructure, electrical and humidity sensing properties of TiO2/polyaniline nanocomposite films prepared by sol–gel spin coating technique, *J. Mater. Sci.: Mater. Electron.*, 2018, **29**, 7099–7106, DOI: 10.1007/s10854-018-8697-9.

34 T. Tene, G. T. Usca, M. Guevara, R. Molina, F. Veltri, M. Arias, L. S. Caputi and C. V. Gomez, Toward large-scale production of oxidized graphene, *Nanomaterials*, 2020, **10**(2), 279, DOI: 10.3390/nano10020279.

35 Z. Lei, L. Lu and X. S. Zhao, The electrocapacitive properties of graphene oxide reduced by urea, *Energy Environ. Sci.*, 2012, **5**, 6391–6399, DOI: 10.1039/C1EE02478G.

36 Q. Zhang, K. Zhang, D. Xu, G. Yang, H. Huang, F. Nie, C. Liu and S. Yang, CuO nanostructures: Synthesis, characterization, growth mechanisms, fundamental properties, and applications, *Prog. Mater. Sci.*, 2014, **60**, 208–337, DOI: 10.1016/J.PMATSCI.2013.09.003.

37 H. Wang, Q. Pan, J. Zhao, G. Yin and P. Zuo, Fabrication of CuO film with network-like architectures through solution-immersion and their application in lithium ion batteries, *J. Power Sources*, 2007, **167**, 206–211, DOI: 10.1016/j.jpowsour.2007.02.008.